PHYSICAL REVIEW C VOLUME 52, NUMBER 2 AUGUST 1995

ARTICLES

Measurement of $np \rightarrow pp\pi^-$ at 443 MeV

M. G. Bachman* and P. J. Riley
University of Texas at Austin, Austin, Texas 78712

P. W. Green and E. Korkmaz†
University of Alberta, Edmonton, Alberta, Canada T6G 2U1

D. J. Margaziotis
California State University, Los Angeles, California 90032

B. W. Mayes, L. S. Pinsky, and Y. Tzamouranis
University of Houston, Houston, Texas 77204

A. Amer, A. R. Berdoz, J. Birchall, J. R. Campbell, C. A. Davis, N. E. Davison,
W. R. Falk, S. A. Page, W. D. Ramsay, A. M. Sekulovitch, and W. T. H. Van Oers
University of Manitoba, Winnipeg, Manitoba, Canada R3T 2N2

D. L. Adams and G. S. Mutchler
Rice University, Houston, Texas 77251

D. A. Hutcheon and C. A. Miller
TRIUMF, 4004 Wesbrook Mall, Vancouver, British Columbia, Canada V6T 2A3

(Received 14 November 1994)

We have measured the relative differential cross section and spin observables for the reaction $np \rightarrow pp\pi^-$ at 443 MeV. Our measurements have been compared with predictions of the model of Kloet and Lomon. Some of the variables show marked disagreement with predictions; for other variables there is surprisingly good agreement.

PACS number(s): 25.10.+s, 25.40.Fq, 25.40.Ve, 13.75.Cs

I. INTRODUCTION

Pion production represents one of the simplest inelastic processes in the nucleon-nucleon system. It sheds light on the N-N and π-N interactions and is key to understanding pion production in more complex systems. Inelasticity accounts for over half the total N-N cross section above 1 GeV, rising quickly from threshold. Any model of the N-N system must be able to simultaneously describe elastic and inelastic scattering above and below pion threshold. Several such models have been proposed for the region 300–1000 MeV [1]. Most are coupled-channel models with the long range part given by pion exchange; the short range is described by heavier meson exchange with appropriate vertex functions, parametrized by cutoffs.

All $NN \rightarrow NN\pi$ reactions are dominated at medium energies by the production of an intermediate resonant Δ which is the major contributor to cross sections. Nonresonant amplitudes may play a significant role, however, in spin observables which are strongly affected by interferences between partial wave amplitudes. For example, using a unitary three-body model, Dubach, Kloet, and Silbar showed in 1987 that nonresonant amplitudes, specifically those from the $T = 0$ initial state, can have dramatic effects on their predictions for spin observables at 800 MeV, while having little effect on their cross section predictions [2]. The nonresonant amplitudes must be taken into account in any attempt to understand pion production except at energies near the Δ resonance.

The $np \rightarrow pp\pi^-$ and $np \rightarrow nn\pi^+$ reactions are well suited for studying the role of nonresonant amplitudes in the inelastic process because the np system is an equal mixture of two isospin channels: $T = 0$ and $T = 1$. From isospin conservation, the Δ resonance ($T = 3/2$) can be fed only from the $T = 1$ initial state; below 1 GeV other resonances ($\Delta\Delta, N^*$, etc.) are too far off-shell to have significant effects. Thus, all partial waves available in the $T = 0$ channel represent nonresonant

---

*Currently at the University of California at Irvine, Irvine, CA 92717.

†Currently at the University of Northern British Columbia, 3333 University Way, Prince George, British Columbia, Canada V2N4Z9.

amplitudes. Further, the $T = 1$ channel can proceed via only the $\Delta^0(J = 3/2, T = 3/2, T_3 = -1/2)$ resonance, much weaker than the Δ^{++} which dominates in $pp \to np\pi^+$ and $pp \to d\pi^+$.

A. $NN \to NN\pi$ isospin formalism

In the isospin notation formalism of Rosenfeld [3], all $NN \to NN\pi$ reactions can be described in terms of three independent cross sections σ_{ij} which represent transitions from initial isospin states i to final isospin states j.

Isospin cross sections		Reaction cross sections
σ_{11}	$=$	$\sigma(nn \to nn\pi^0) = \sigma(pp \to pp\pi^0)$
$\sigma_{11} + \sigma_{10}$	$=$	$\sigma(nn \to np\pi^-) = \sigma(pp \to np\pi^+)$
$\frac{1}{2}(\sigma_{11} + \sigma_{01})$	$=$	$\sigma(np \to nn\pi^+) = \sigma(np \to pp\pi^-)$
$\frac{1}{2}(\sigma_{10} + \sigma_{01})$	$=$	$\sigma(np \to np\pi^0)$

Similar expressions for differential cross sections can also be written, but they are slightly more complicated [4]. If we express the above cross sections in terms of transition amplitudes, such as those defined by Bystricky *et al.* [5], it can be shown that a forward-backward asymmetry in the $np \to pp\pi^-$ (or that of $np \to nn\pi^+$) differential cross section is direct evidence that σ_{01} is nonzero. If charge symmetry is invoked, a difference between $np \to pp\pi^-$ and $np \to nn\pi^+$ differential cross sections is also evidence that σ_{01} is nonzero.

B. Previous measurements of $np \to NN\pi^\pm$

It has been clear for many years that below ~ 2 GeV the $T = 1$ channel is the dominant (and resonant) mode for pion production [6]. Almost all $np \to NN\pi^\pm$ measurements below 1 GeV have sought evidence for $T = 0$ inelasticity, either by (1) directly comparing $np \to NN\pi^\pm$ results to $pp \to pp\pi^0$ (pure σ_{11}) at the same energy, or (2) looking for asymmetries (π^+-π^- or forward-backward) in differential cross sections.

Two papers [5,7] have attempted global fits to all the known $NN \to NN\pi$ total cross section data in order to calculate the resulting independent isospin cross sections by addition or subtraction. The results are inconclusive. A plot of available published reaction cross sections for $np \to NN\pi^\pm$ below 1 GeV [8–18] is shown in Fig. 1. Also shown is Arndt's estimate for $\frac{1}{2}\sigma_{11}$ (lower solid curve) based on measured cross sections for $pp \to pp\pi^0$ up to 1 GeV. Except for a few data points, the np total cross sections appear to fall along the $\frac{1}{2}\sigma_{11}$ curve. Arndt [7] concludes that the $T = 0$ inelasticities are essentially zero below 1 GeV; Bystricky [5] disagrees with this conclusion. Both papers point out the need for better cross section data. Figure 2(a) shows published cross section measurements for $pp \to pp\pi^0$, taken from the work of Stanislaus and others [19–23]. We have compared $np \to NN\pi^\pm$ cross sections with those for $pp \to pp\pi^0$ by fitting the data and subtracting the fit from $2\sigma(np \to NN\pi^\pm)$. The results, shown in Fig. 2(b), are in general consistent with zero for σ_{01}, in agreement with the conclusion of Arndt.

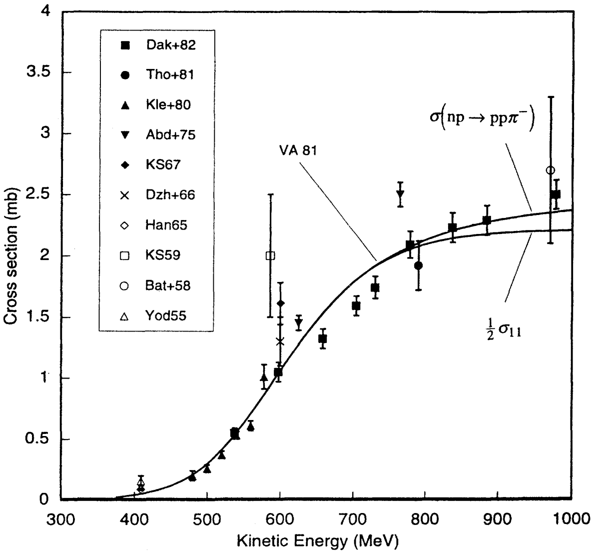

FIG. 1. Published reaction cross sections for $np \to NN\pi^\pm$ below 1 GeV. Also shown is Arndt's estimate for $\frac{1}{2}\sigma_{11}$.

In contrast to the total cross section data, most $np \to NN\pi^\pm$ differential cross section measurements do claim evidence for $T = 0$ in their data. Both Yodh [8] and Handler [11] claim a forward-backward asymmetry at 409 MeV. Measurements by Soviet physicists at JINR found evidence for $T = 0$ from $\pi^\pm$ differential cross sections which differed from corresponding $pp \to pp\pi^0$ data [12,13]. Kleinshmidt [15] found similar results. The anisotrophy is expressed in the form of an anisotrophy parameter b, which describes the pion angular distribution, above 300 MeV, in terms of

$$\frac{d\sigma}{d\Omega} \propto \tfrac{1}{3} + b\cos^2\theta^*_\pi .$$

We have made a compilation of the b parameters as a function of energy. These are shown plotted in Figs. 3(a) and 3(b) for $np \to NN\pi^\pm$ and $pp \to pp\pi^0$, respectively. The data clearly indicate that b is nonzero for $np \to NN\pi^\pm$ in the 400–600 MeV range, while it is consistent with zero (or a very small value) for $pp \to pp\pi^0$. It is interesting that in this same energy range (for energies above the 409 MeV data of Handler) there appears to be no evidence for forward-backward asymmetry in π^+ versus π^- yields, indicative of a negligible cosine term in the expression for $d\sigma/d\Omega$. This could be explained if the $T = 0$ amplitudes are out of phase with respect to the $T = 1$ amplitudes.

Despite the strong evidence provided by the differential cross section data, the inelasticity in $T = 0$ is usually considered negligible in phase shift analyses below 1 GeV [24], probably because of the apparent zero value for σ_{01} from the integrated cross section data. As can be seen from the data in Fig. 1, the integrated cross sections are not all consistent, particularly in the region of 600–800 MeV. The null result for σ_{01} may be a statement of the difficulty in doing these measurements as much as a measure of the $T = 0$ inelasticity.

A third way to probe the $T = 0$ amplitudes is with spin observables. There have been few measurements of spin dependent observables for $np \rightarrow pp\pi^-$, mostly because of the difficulty in obtaining a polarized neutron beam of high quality. Terrien *et al.* [25] made analyzing power measurements A_{NO} at beam energies of 572, 784, 1012, and 1134 MeV. The analyzing powers were calculated in bins of invariant p-p mass and pion angle in the center-of-momentum system (CMS). Since a 4π detector was used, Terrien's results represent weighted integrals over the remaining phase space variables. In this paper we report similar measurements of A_{NO}, A_{SO}, and A_{LO}, as well as relative $d\sigma/d\Omega$ for a neutron beam energy of 443 MeV.

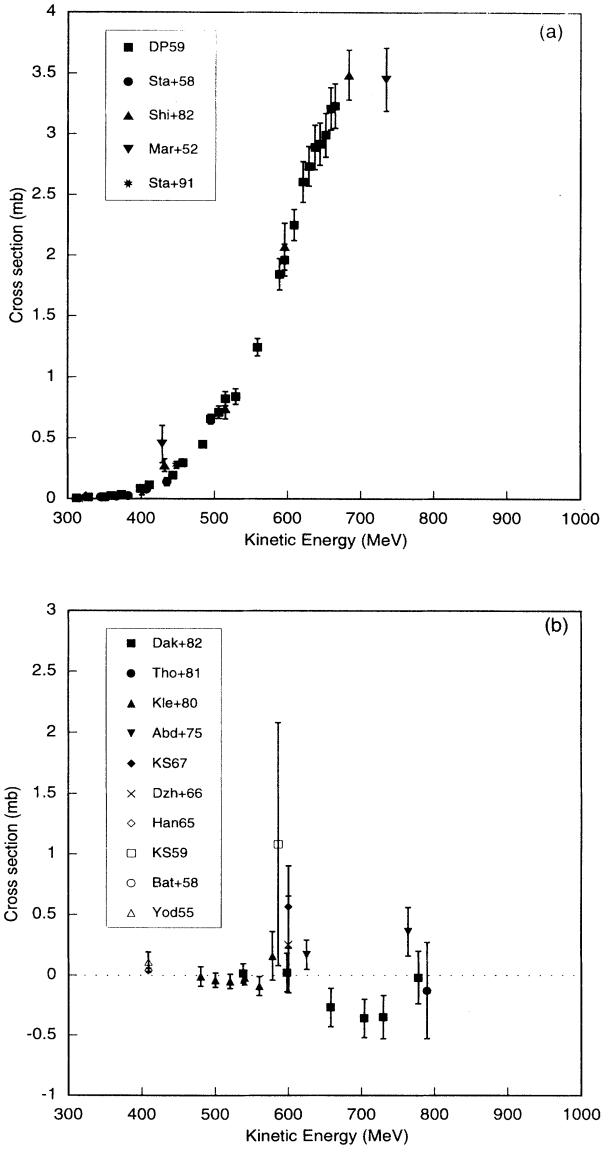

FIG. 2. Total cross sections for $pp \rightarrow pp\pi^0$ below 1 GeV (a). Estimates for σ_{01} based on subtraction of cross sections (b).

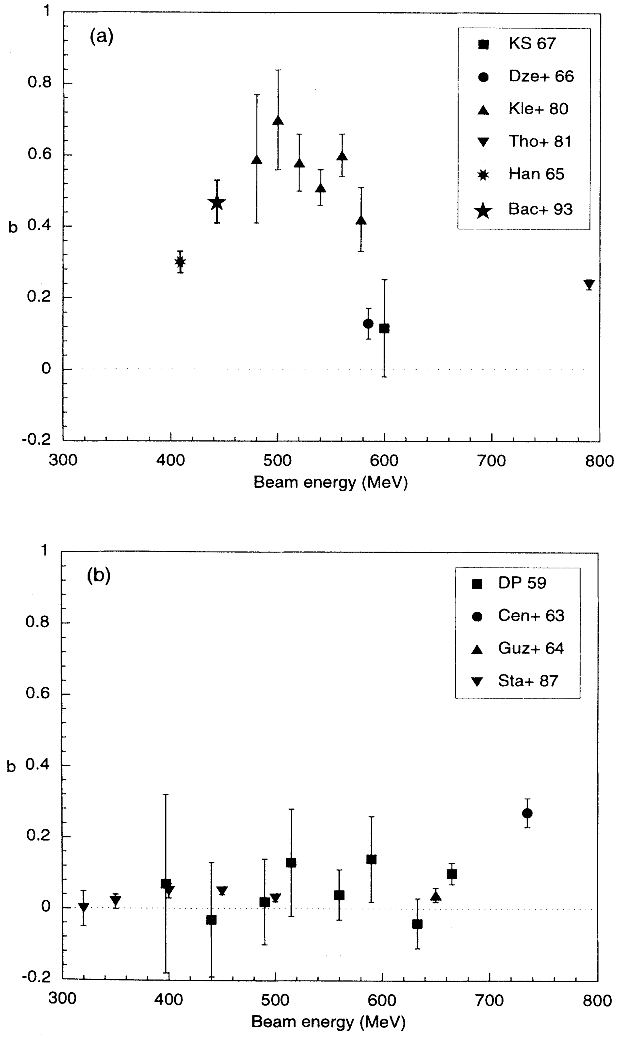

FIG. 3. Plots of anistropy parameters b, for (a) $np \rightarrow NN\pi^{\pm}$ and (b) $pp \rightarrow pp\pi^0$. The data point for the present work at 443 MeV in (a) is given the label [$Bac + 93$].

For the asymmetries, A_{iO}, the first index, $i = S,\ N,\ L$, refers the beam polarization (x, y, z) with respect to a pion scattering in the xz plane. Thus, for example, A_{NO} is the scattering asymmetry which corresponds to a pion scattering in the positive xz plane, and a beam polarization in the positive y direction. Further details may be found in Ref. [26].

II. THE EXPERIMENT

The experiment was performed using the polarized neutron beam facility available at the TRIUMF cyclotron. The neutron beam was scattered from a liquid hydrogen target and the subsequent charged reaction products (protons and pions) measured in large acceptance drift chambers and a partial cylindrical array of scintillator bars. Trajectories, times-of-flight, and pulse heights were measured for the charged particles and kinematic events were reconstructed using this information. Yields and asymmetries were extracted and binned as functions of various coordinate variables.

A. The beam

A schematic of the TRIUMF beamline is shown in Fig. 4. The polarized neutron beam was obtained by scattering polarized protons [27] from a liquid deuterium production target (LD_2). The proton polarization was typically 45–50 % and was reversed for half the polarized beam cycle. A special tuning procedure provided a narrow, pulsed 457 MeV proton beam of 450 ps FWHM every 43 ns [28]. The proton intensity at the LD_2 target was typically 500 nA which resulted in approximately 1 million neutrons per second at our target, 12.6 m downstream. The tight bunching of the proton beam allowed for clean extraction of the quasifree neutrons from the inelastic neutral background. The neutron beam energy was checked by the kinematics of three-body final state events (where the kinematics are constrained by conservation of energy and momentum) and found to be 443±3 MeV.

The 457 MeV proton beam passed through two proton polarimeters and then through a superconducting, solenoidal magnet (JANIS) which precessed the polarization from normal to sideways. The quasifree reaction $p + d \to np + (p)$ has a spin transfer coefficient, $K_{SS} = -0.8066$ and $K_{SL} = -0.0125$ at 9° for 457 MeV incident protons [29]; neutrons exiting at 9° had polarizations of typically 32–35 % in the sideways direction. A magnet downstream of the LD_2 production target swept away charged particles and precessed the neutron polarization by 21.3°. The 9° neutron beam was collimated and then passed through two dipole precessing magnets (CLYDE, BONNIE) which could be set to align the beam in any of S, N, or L polarizations.

The liquid hydrogen target, the experimental detector, and additional beam monitors were downstream of these magnets. Neutron beam polarizations were calculated using the proton polarimeters and magnet settings, and then checked for consistency by the asymmetry in the neutron polarimeters. Due to the nonzero K_{SL}, the neutron beam polarization was not exactly N (or S or L) for cases when the proton beam polarization was reversed. However, all precessions of the neutron spin were calculated for the beamline, and thus the exact direction of the polarization vector was known for all beam polarizations. Agreement among all polarimeters (proton and neutron) was excellent, and well within the precision of all polarimeters. Uncertainty for transverse neutron polarization is estimated at ~ 3%; uncertainty in the L-type beam is slightly higher (~ 4%) because the neutron polarimeter cross check was not available.

As a further check, we calculated the analyzing power for a subset of $np \to np$ events in our experimental detector. The result compared with Arndt's phase shift solution [30] is shown in Fig. 5. Agreement is very good. Error bars are statistical only, even though some systematic uncertainties arise (up to ~ 10%) for very large neutron angles because the np elastic signature was not as

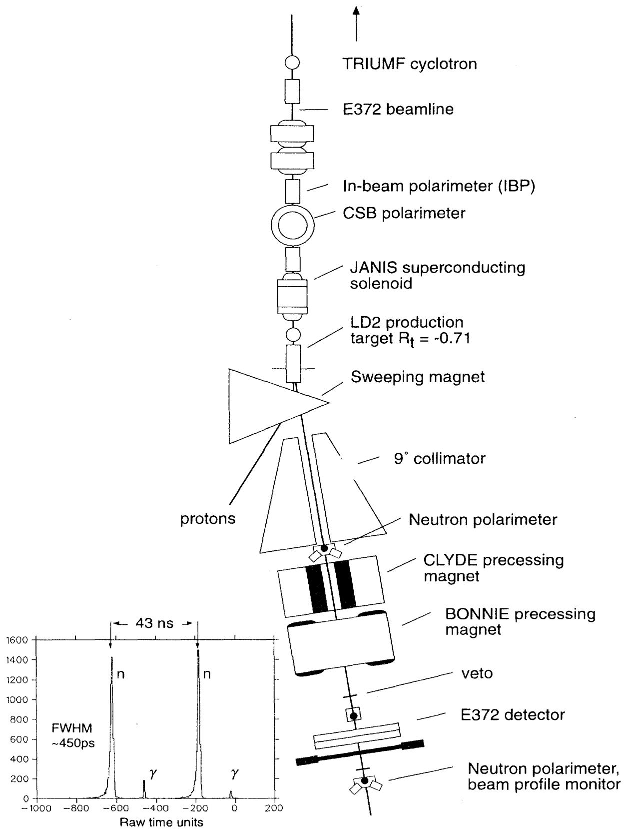

FIG. 4. A schematic drawing of the polarized neutron beam-line at TRIUMF. Also shown is the time structure of the neutron beam.

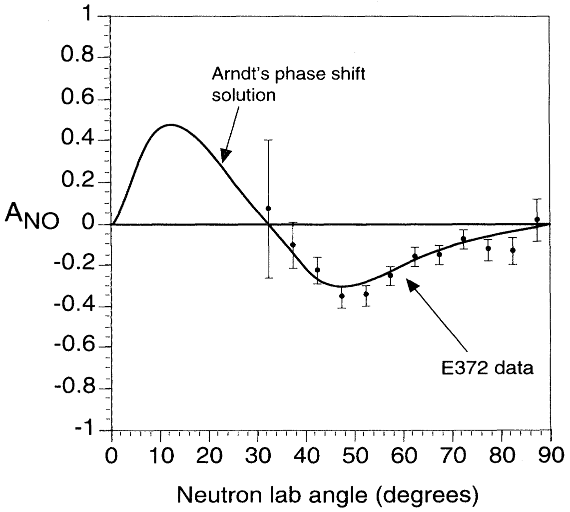

FIG. 5. The analyzing power for a subset of elastic np scattered events in our detector compared with Arndt's phase shift solutions.

clearly identifiable for those angles. The method for calculating the $np \to np$ A_{NO} was identical to the method we used to calculate the $np \to pp\pi^-$ asymmetries.

B. The experimental setup

Figure 6 shows a diagram of the target and detector. The 5 mil kevlar mesh liquid hydrogen target flask was cylindrical, of diameter 5 cm and height 16 cm, enclosed within a vacuum chamber. Most of the exiting charged particles passed through a large downstream window in the vacuum chamber fabricated with 3 mil kapton plus 8 mil mylar. We taped ~ 25 million events, about 1/3 of these with the target empty.

The detector was built around the known kinematics of $np \to pp\pi^-$ at 443 MeV. At this energy, the protons are constrained to be emitted within a lab half-angle of 42°. Two large drift chambers and a scintillator hodoscope array (S_1 and S_{bar}), subtending a half-angle of $\sim 45°$ at the target, measured the directions and velocities of the charged particles. This information allowed the kinematics of each event to be reconstructed. For "three-track" events (three tracks in our detector, where the pion goes forward into the detector), there is little background competition, since there are few neutron induced processes that can produce three charged particles in the final state. Our acceptance for these events was limited to the case where three separate scintillator bars were hit. For "two-track" events, there was considerable competition from quasifree $nn \to np\pi^-$ events originating in the target walls, vacuum windows, and timing scintillator, S_1. Nevertheless, through good kinematic analysis we were able to reject most background events for both two-track and three-track events. The final data set consisted of roughly 400 000 good $np \to pp\pi^-$ events distributed over N, S, and L states. For these events background constituted only about 4% of the total.

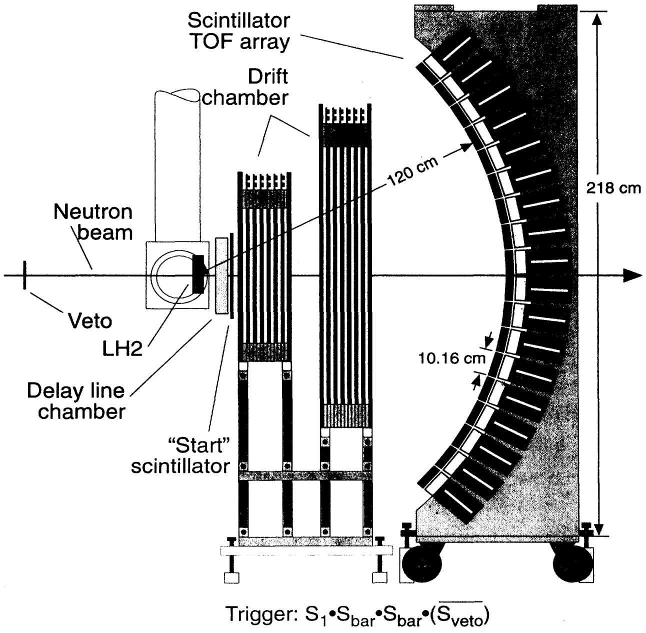

FIG. 6. A schematic diagram of our $np \to pp\pi^-$ detector at TRIUMF.

There were also various calibrating devices in our detector system: small "button" scintillators which sat behind the scintillator bars; small axial detectors which were accurately placed in the center of the beam axis; two side MWPC's for detecting backward going pions. These devices were associated with their own triggers which could override the main trigger and were used to pinpoint and simplify calibrations. In order to reduce the fraction of events originating downstream of the target, particularly in S_1, a low mass delay line chamber was placed between the target and S_1. The chamber was used simply as a thin logic device (TLD) to signal passage of a charged particle; it was not used to obtain position information.

The event trigger for the experiment consisted of three levels: 0, 1, 2. The level 0 trigger consisted of a pulse from a single photomultiplier in any bar; it provided the common "start" for all TDC's and the "stop" for the drift chamber electronics. The level-1 trigger, shown in Fig. 7, required that (1) the computer be ready for data, (2) a second bar fired, (3) the S_1 fired, (4) the TLD fired and (5) no VETO. A crude pattern recognition which vetoed events for which only bars in the upper half or the lower half of S_{bar} fired was also included. If the level-1 condition was not fulfilled, a fast clear was sent to all electronics and all registers were cleared. The level-1 trigger was built around the LeCroy NIM module 380A Multiplicity Logic Unit (MLU), which allows multiple inputs (up to 32) and has outputs which set a "true" when the condition that $= N$ is satisfied (or alternatively when $> N$ is satisfied), where N ranges from 0 to 6. The level-2 trigger was a software trigger written in the $J11$ ("Starburst") preprocessor which was responsible for buffering the data and sending it to the acquisition computer (a VAX 750; later a VAX 780) for spooling on to 8 mm tape. This level-2 trigger required that (1) the event time with respect to the RF corresponded to the neutron pulse, (2) the events were not from the central regions of the two center bars, and (3) there were more than 12 wire chamber hits registered. These cuts in the trigger were designed to eliminate γ-induced events or single track events which mimicked a two-track event by double scattering through two adjacent bars. The $J11$ preprocessor buffered the variable length events (typically 340 bytes each) in its 16K memory, then dumped the buffer to the VAX 780. The buffering was done at a rate of about 2 ms per event; the dumping took about 100 ms. Event collection was typically 140 Hz, limited by acquisition speed. We ran at typically 40–50 % dead time.

Although in principle our trigger was clean, we found much contamination from competing reactions with much higher cross sections than for $np \to pp\pi^-$. The major reactions contributing to false triggers were $np \to np$ elastic and inelastic $n(n) \to np\pi^-$ events. Elastic events should have been rejected since they usually hit only one bar; however, approximately 4% of the time a single track would produce pulses in two bars via scattering from one

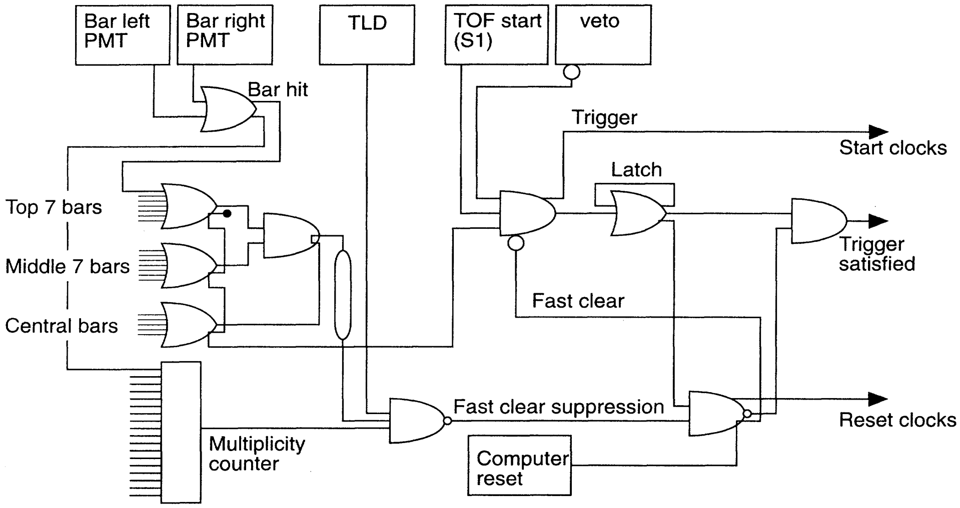

FIG. 7. The level-1 trigger. All timing was done with respect to the photomultiplier of the first bar to record an event.

to an adjacent bar, leading to a false level-1 trigger. The drift chambers were found to suffer from crosstalk, implying that the level-2 trigger (which counted chamber hits) was also often satisfied. The $n(n) \to np\pi^-$ events originated from quasifree scattering from the target walls and from other target materials, including the S_1 scintillator. Since this reaction has two charged particles in the final state, it satisfied all the trigger requirements. Events originating in scintillator S_1 should have been vetoed by the delay line chamber between the target and S_1, but the efficiency of this detector was such that a significant number of events originating downstream of the chamber managed to satisfy all the triggers. About 55% of the two-track events came from materials other than the LH_2 target.

The scintillator array provided timing and pulse height information. The array consisted of 18 NE104 plastic scintillator bars, each $200 \times 10.4 \times 3$ cm^3, in a curved array 120 cm from the target. Each bar was viewed at both ends by TRIUMF standard Phillips XP2230 phototubes. The usual optimizing of the system (gain matching, voltage plateauing, etc. was done. Software calibrations were based on np elastic data where the kinematics are fully constrained. Conversions from TDC and ADC units to standard units (nanoseconds, MeV) were found through extensive calibrations and revealed that the system had better than $\sigma = 240$ ps timing resolution, and $\sigma = 3$ MeV energy resolution for all bars. The time difference between the arrival time of a charged particle in a bar and its time of passage through S_1 provided velocity information; the pulse height information helped in particle identification and acted as a further constraint in the kinematic reconstruction. Figure 8 shows a plot of velocities versus energy loss in the bars. The correlation follows the expected Bethe-Bloch relationship at proton kinetic energies greater than 70 MeV; the leading edge of the distribution represents protons which stopped in the bars and deposited all their energy. Proton and pion events are identifiable by inspection. Protons appear as events with slower velocities, losing more energy in the plastic scintillator; pions are the faster events with smaller energy loss.

The tracking detector consisted of two large drift chambers, with active areas of 59.5×22.0 in^2 and 59.5×42.0 in^2. Each chamber had six sense planes with wires running in the following coordinate directions: $UYXXUY$. The U direction is 45° to X and Y and helped resolve the ambiguities created by multiple tracks. The sense wires were made of 1 mil gold-plated tungsten and were 2 in apart connected to individual preamps, discrimators, and TDC's. Drift resolution was ~ 0.6 mm; the efficiency per plane was typically 96%. The drift times were read and encoded using LeCroy 4290 digitization electronics and the data words appended to the end of the event buffer. The layout and specifications of the drift chambers are indicated in Fig. 9.

Track reconstruction through the detector turned out to be the most difficult and most CPU intensive aspect of the analysis. Multiple tracks through the detector gave rise to problems of high combinatorics, especially with events that had crosstalk. Furthermore, the large cell size (2 in) resulted in many tracks sharing cells and so making them difficult to resolve. An approach using template matching followed by full combinatoric fitting was used. In this method, a set of templates recording all the possible cell patterns which correspond to physical tracks is stored as an indexed list in memory. Each cell pattern was indexed in terms of which scintillator bar its corresponding trajectory was associated with, and where on the bar it intersected. When this was completed, we had in the form of a large indexed file every physically allowable set of cell patterns which could lead to a track. The term *physically allowable* implies that the line of interest must pass through (and not just close to) the corresponding finite-sized cell. A measured pattern is compared to the list and the best candidates are kept. A candidate consisted of a subset of cell patterns or templates corresponding to a particular position and scintillator bar; the more cells which matched the data, the higher the score of the candidate. After this initial screening, a least squares

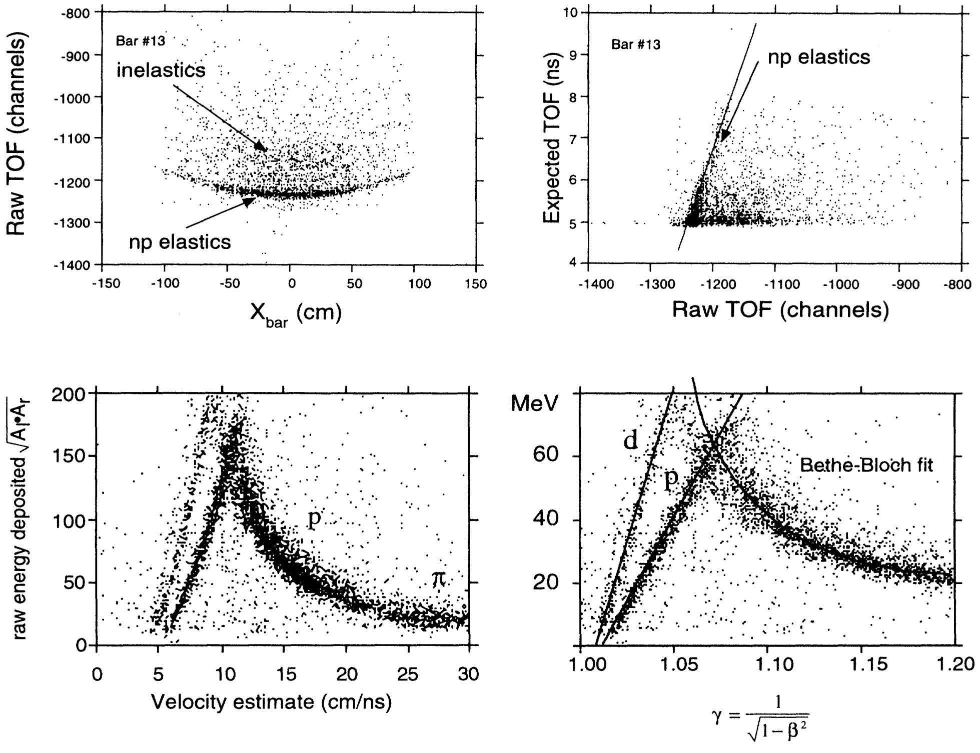

FIG. 8. Scintillator bar performance. The top figures show time-of-flight as a function of bar position (where $x = 0$ is the center of the bar), and a comparison to expected $np \rightarrow np$ values at 443 MeV. The bottom figures show plots of energy deposited in the scintillator versus particle velocity.

line fitting procedure was employed to resolve the left-right ambiguity of a track with respect to a given drift chamber wire. Finally, a preliminary vertex was calculated from the tracks (if there was more than one track) and the tracks were refitted using the extra data point at the vertex. The uncertainty in the vertex was given by the RMS distance of closest approach. Vertex reconstruction based on tracking allowed us to eliminate most of the background based on target cuts.

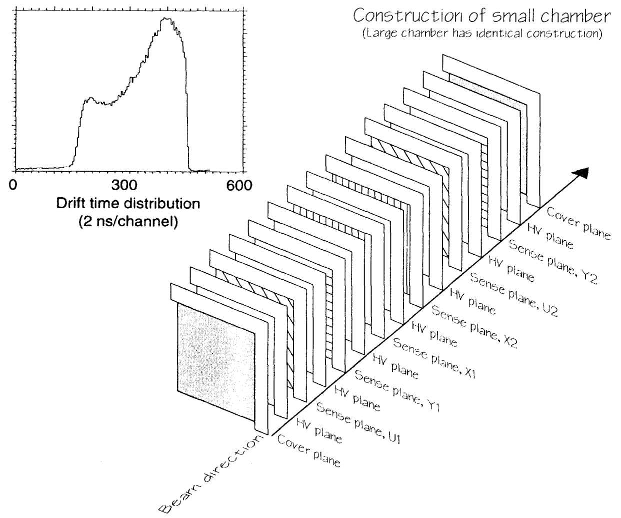

FIG. 9. Time distribution and layout of the $E372$ drift chambers.

Single track efficiency was ~ 98%. Cleanly separated multiple tracks had typical efficiencies of ~ 89% for two tracks, ~ 85% for three tracks. However, multiple-track efficiency overall was lower because it depended on the relative angles of the tracks and the cuts applied in the tracking algorithms. Vertices were calculated for multiple tracks and found to have RMS deviations of less than 1.03 cm for 67% of the multiple-track events. A plot of these vertices for an empty target run (for $\sigma_{\mathrm{vertex}} < 1.0$ cm) is shown in Fig. 11(a).

III. EVENT ANALYSIS

Raw events were written to 8 mm tape for storage and later reduction. Four event types were written to tape: events 1, 2, 3, and 6. Beam monitors, polarization monitors, photomultiplier tube voltages, and various clocks were scaled by 24 bit scalers; these were ready every 5 s and written to tape as event 1. Beam profile monitor events, event type 3, were prescaled, usually by a factor of 10^{-3}, before being written. Beam timing and position monitor events, type 6, were fed to our computer every 2 min. Type-2 events were those triggered in our detector, and constituted the bulk of the data on tape.

A total of ~25 million type-2 (not calibration/monitoring) events, written to 8 mm tapes, were taken in two data runs. The analysis of data tapes followed the flow chart shown in Fig. 10. Because the analysis was CPU intensive, taking ~ 1 s/event on a VAX station 3100 (for event-2 data), jobs were run on several different machines simultaneously. The greatest effort in

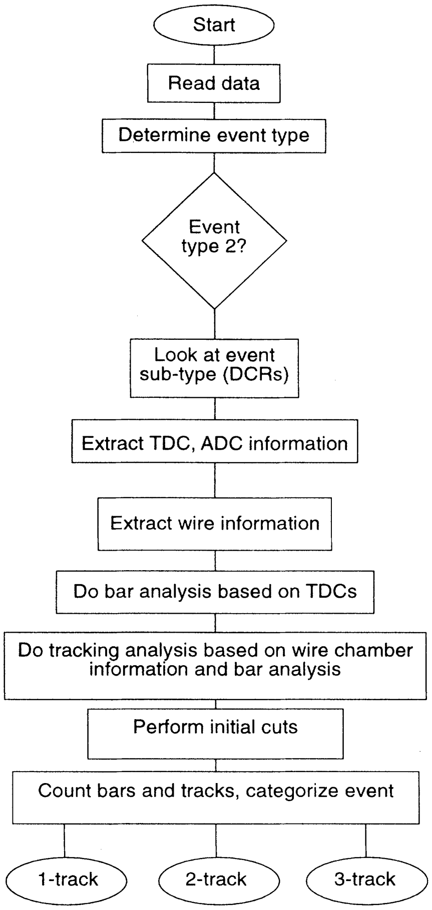

FIG. 10. A flow chart of the $E372$ event data analyses.

the analysis was the tracking which performed the pattern recognition algorithms and the fitting of tracks passing through the wire chambers. What remained after this was to determine the kinematics of each event using TDC and ADC information, and to bin appropriately. Using this information, we were able to reconstruct the kinematics of each event, and then, by using cuts based on kinematic criteria, to select only the $np \to pp\pi^-$ data. Events were classified into three types; one-, two-, and three-track events; the kinematic analysis was different for each.

A. Reconstructing kinematics

The kinematics for each event were determined from the measurements of track angles, times-of-flight, and energy loss in the bars. For three-track events, conservation of energy and momentum are sufficient to accurately calculate the kinematics based on angles alone. For two-track events, a solution for the momenta of the two particles and the identity of the particles had to be determined in an iterative fashion. A kinematic χ^2 was defined by

$$\chi^2(p) = \frac{(\mathrm{TOF}_1 - \mathrm{tof}_1)^2}{\sigma^2_{\mathrm{TOF}}} + \frac{(\mathrm{TOF}_2 - \mathrm{tof}_2)^2}{\sigma^2_{\mathrm{TOF}}} + \frac{(dE_1 - de_1)^2}{\sigma^2_{dE}} + \frac{(dE_2 - de_2)^2}{\sigma^2_{dE}}.$$

Here, the upper case variables (TOF, dE) represent the measured quantities. The lower case variables (tof, de) represent the estimated quantities which depend on the adjustable parameter p, the momentum of one of the tracks. An initial value for p was determined using the time-of-flight associated with the particle and a guess as to the particle's identity. With these values for the first particle, the momentum of the second particle could be calculated using the quadratic expression

$$p_2 = \frac{-B \pm \sqrt{B^2 - 4AC}}{2A},$$

where A, B, and C are defined by

$$A = \frac{[(\vec{p}_{\mathrm{lab}} - \vec{p}) \cdot \hat{e}]^2}{(E_{\mathrm{lab}} - E)^2} - 1,$$

$$B = \frac{[m_2^2 - m_3^2 + (E_{\mathrm{lab}} - E)^2 - |\vec{p}_{\mathrm{lab}} - \vec{p}|^2][(\vec{p}_{\mathrm{lab}} - \vec{p}) \cdot \hat{e}]}{(E_{\mathrm{lab}} - E)^2},$$

$$C = \frac{[m_2^2 - m_3^2 + (E_{\mathrm{lab}} - E)^2 - |\vec{p}_{\mathrm{lab}} - \vec{p}|^2]^2}{4(E_{\mathrm{lab}} - E)^2} - m_2^2,$$

$E_{\mathrm{lab}}, \vec{p}_{\mathrm{lab}}$ = total lab energy and momentum, $E, \vec{p}$ = given particle's energy and momentum, $\hat{e}$ = unit vector of second track direction.

In order to take into account all the information available, it was necessary to calculate the times of flight and pulse heights for the two particles. After the kinematics for a particular p were determined, the particles were "propagated" through an imaginary detector designed to mimic the effects of the actual detector. The resulting times-of-flight and energy losses (tof, de) were input in the χ^2 defined above. This process was repeated for different p until the χ^2 was minimized. Minimization was typically done in three to six iterations. However, the quadratic expression has two solutions and there are three unknown particle identities, so the minimization was repeated six times for each solution and each particle combination.

This χ^2 minimization depended strongly on our ability to mimic the detector in software. Extensive calibrations were done on the tof and *de* routines to ensure accuracy. The results shown in Figs. 11(b) and 11(c) suggest that this χ^2 technique was both accurate and effective. In Fig. 11(b), we show the vertex reconstruction for events with good reduced $\chi^2 (< 1.0)$ and those with poor reduced $\chi^2 (> 3.0)$. The poor χ^2 are correlated with the walls and background materials, as expected for events originating from bound protons in carbon with associated Fermi motion. Good χ^2 are correlated with the free hydrogen. In Fig. 11(c), we show the result of the particle identification (which comes from the kinematic minimization). The two-track events which reconstructed as πp events are strongly correlated with the target walls and background. This is consistent with the hypothesis that the background is mostly $nn \rightarrow np\pi^-$, which has a large cross section. On the other hand, $np \rightarrow pp\pi^-$ events are strongly correlated with the LH_2 region. The final cut on the data was the following: (1) at least two protons, (2) $\chi^2/N < 2.0$, and (3) a vertex within the LH_2 target region ($r_{xz} < 2.5$ cm). The full series of triggers and cuts were quite stringent and only 3% of the data taken with the target filled passed all the criteria imposed. For target empty runs, almost no events satisfied the cuts. Comparison of results obtained with the target full and the target empty indicated that after all cuts had been applied, background constituted only 4.3% of the accepted events with the target full.

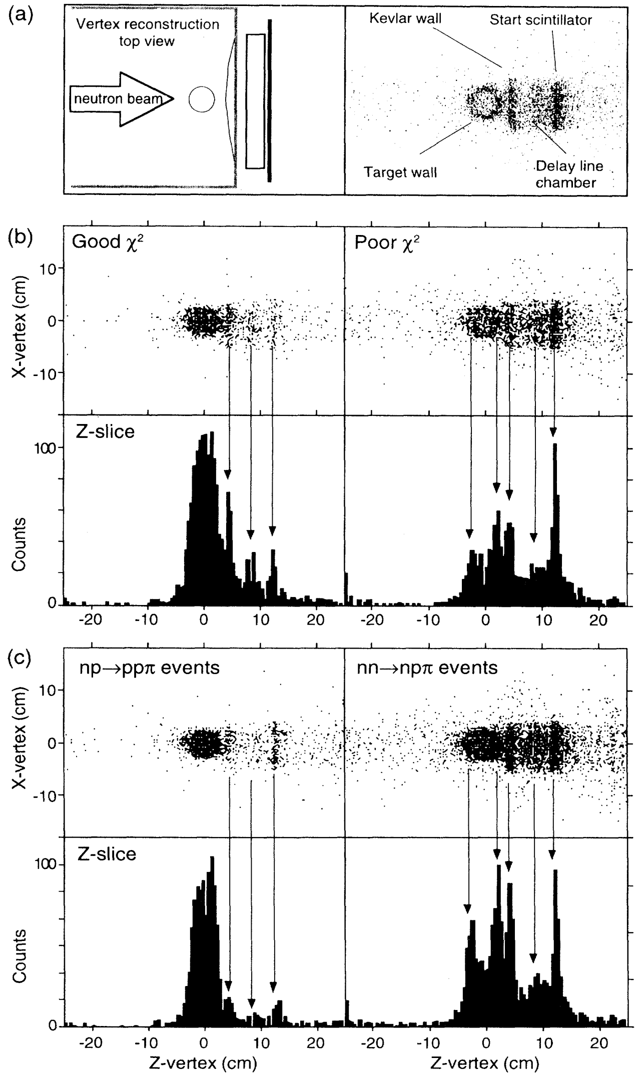

FIG. 11. Event vertices correlated with cutting parameters. (a) Track vertices for an empty target run, suggesting the correct fiducial cuts. (b) Vertex reconstruction for events with good reduced χ^2 (< 1.0) and those with poor reduced χ^2 (> 3.0). (c) Vertex reconstruction using particle identification to distinguish $np \rightarrow pp\pi^-$ and $nn \rightarrow np\pi^-$ event. Slices are shown projected onto the z axis.

B. Estimating observables

The event analysis resulted in a clean set of data of good kinematic accuracy, but the acceptance over phase space is difficult to estimate realistically. A series of Monte Carlo simulations were performed and subjected to the same analysis as the actual data. From this, two efficiency functions were found, one for the two-track events and one for the three-track events. Since these classes of events were analyzed differently, their efficiency functions were different. Events were binned and corrected using these functions. The resulting relative differential cross sections for the two-track and three-track events matched over phase space regions where both efficiency functions were reliable. In regions where this was not true, however, the two- and three-track relative cross sections did not always match, and in such case the cross section corresponding to the more reliable correction function was chosen as correct. Statistical error is small; the error bars in the associated plots (Fig. 14) are estimates of systematic errors which result from uncertainty in the correction functions.

The dominant uncertainties associated with the correcting efficiency functions (and hence, the data) come primarily from difficulties in estimating systematic tracking error, particularly in the case of electronic noise. While the tracking was quite good at seeing through noise in the drift chambers overall, for regions of phase space where tracks were emitted close together, the tracking algorithms could be fooled. In these regions, the efficiency function varied greatly with the model of electronic noise used, and for that reason, the uncertainty in the data is higher. For a small region of phase space, the efficiency function could not be considered reliable and the corresponding relative cross section data was not determined.

Asymmetries were calculated from the data set and are of much higher quality than the differential cross sections. This is because the method used in calculating the asymmetries required no external correction function. Instead, a likelihood function using the known average beam polarization vector was used to calculate the spin observables on an event-by-event basis. Since the detector was symmetrically efficient, and since we reversed polarizations often, this method resulted in accurate measurements of asymmetries.

The probability of detecting an event is defined in terms of the analyzing power and beam polarization (P) as

$$p(\vec{\rho},\phi,\vec{P}) = \left(\frac{d\sigma}{d\rho}\right)\varepsilon(\phi)\varepsilon(\vec{\rho})\varepsilon(\vec{P}) \times[1 + A_{SO}P\cos(\phi_P-\phi) + A_{NO}P\sin(\phi_P-\phi) + A_{LO}P_z],$$

where $d\rho$ = an element of phase space (not including ϕ), $\varepsilon(\phi), \varepsilon(\vec{\rho})$ = detection efficiencies at ϕ and $\vec{\rho}$, $\varepsilon(\vec{P})$ = the probability that the beam has polarization $\vec{P}$.

The angles are defined in Fig. 12. This expression assumes negligible background. This equation is similar to those given by other authors (see Shypit [31], for example), except that our expression is valid for beam polarizations and analyzing powers in arbitrary directions. For the transverse polarizations, we maximized the likelihood function which corresponds to the above probability in terms of parameters A_{NO} and A_{SO}, solving for both simultaneously. This was accurate to second order under the assumption that the detector is symmetrically efficient, i.e., $\varepsilon(\phi) = \varepsilon(\pi-\phi)$, or that the net beam polarization averaged to zero. Both conditions were true for our experiment.

The uncertainty in analyzing power was estimated by searching for the 67% probability limits, approximately given by the usual expression

$$\sigma \approx \sqrt{\frac{1-(AP)^2}{N}}.$$

This method for estimating the asymmetries has the advantage that the beam polarization need not be constant over long periods of time. It requires no binning over angles (ϕ) and subsequent subtractions. Furthermore, it solves for A_{NO} and A_{SO} simultaneously. We used this estimation technique for all A_{SO} and A_{NO} measurements, including the $np \to np$ calibration data shown in Fig. 5.

Estimates of the accuracy of this technique can be gauged by looking at A_{SO} and A_{NO} plots projected to $\cos(\Theta)$ and $\cos(\Psi_{pp})$. By parity arguments, A_{SO} are expected to be zero in these plots. However, the calculation of A_{SO} and A_{NO} are completely identical and simultaneous—no distinction is made between the two quantities. A systematic error in detector efficiency or polarization direction would appear in A_{SO}. As is seen in Figs. 15 and 16, A_{SO} remains zero everywhere.

For A_{LO}, we calculated an asymmetry between yields for longitudinal polarization "normal" and "reverse." This technique is less than ideal since systematic errors may come in from nonzero transverse components in the beam polarization. Relative systematic error for A_{LO} is estimated at 1–2 %.

IV. RESULTS AND DISCUSSION

The observables are presented in terms of four kinematic variables: $M_{pp}, \cos\theta, \cos\Psi, \chi$, which are illustrated in Fig. 13. The scattering plane azimuthal, $\phi = \phi_\pi$, serves only to rotate the reaction frame with respect to the lab frame, and so is not inherently interesting. M_{pp} is the invariant mass of the p-p system. The angular variables are independent and represent equal volumes of accessible phase space. θ and ϕ are the polar angles of the pion in the center-of-mass system. The variables Ψ and χ are polar angles defined for the fast proton in the decay frame of the p-p system; $\cos\Psi$ has range 0–1.

A. Differential cross sections

Relative differential cross sections, projected to a single variable, are shown in Fig. 14. We have normalized our data to a total cross section of 0.1 mb, which was estimated from the curve on Fig. 1. Also shown are predictions of Kloet and Lomon [32] based on T matrices provided to us (dashed line). The dotted line is a pure phase space prediction; the dotted-dashed line is the effective efficiency function, shown with arbitrary normalization.

We find a strong $\cos^2\theta$ dependence, as did Kleinshmidt and Thomas at higher energies. This can be fit to a polynomial of the form $d\sigma/d\Omega \sim 1/3 + bx^2$, where $b = 0.47 \pm 0.06$. We have plotted this value in Fig. 3(a); it is consistent with the older data and adds to the evidence that the anisotropy parameter for $np \to NN\pi^\pm$

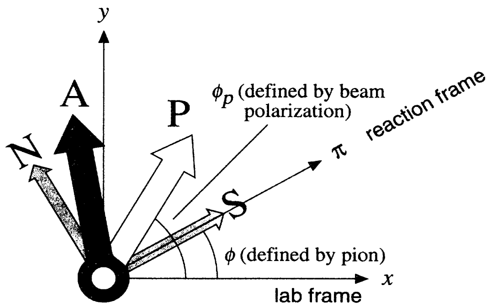

FIG. 12. The coordinate system and angles used in the calculation of asymmetries.

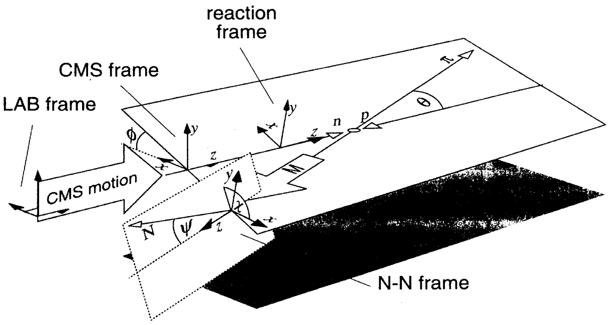

FIG. 13. The kinematic variables used in defining and binning the observables.

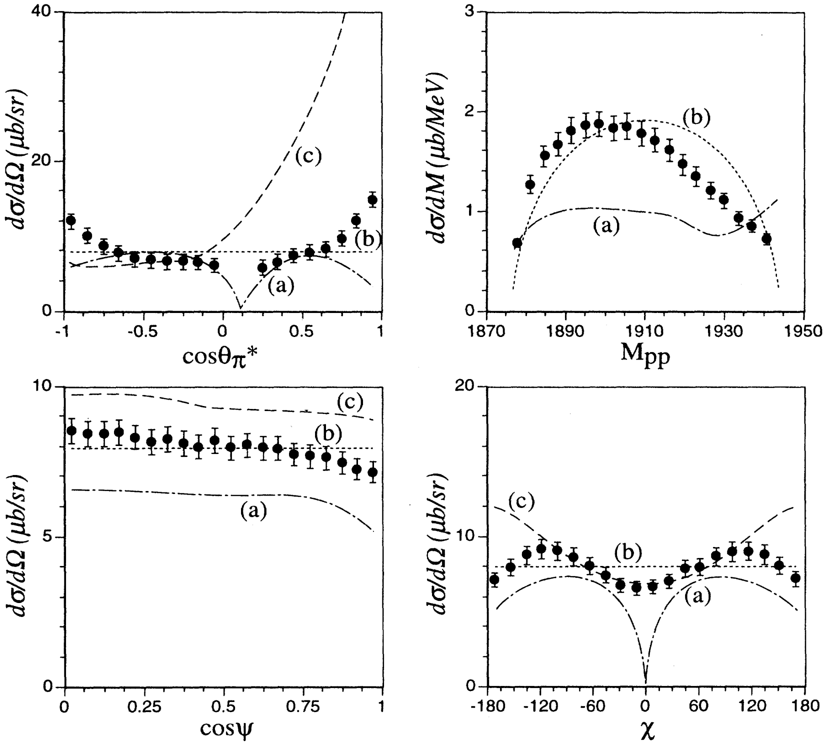

FIG. 14. Relative differential $np \to pp\pi^-$ cross sections. The data are normalized to a total cross section of 0.1 mb. The dot-dashed line (a) is the effective efficiency function (arbitrary normalization); the dotted line (b) is a pure phase space prediction (same normalization); the solid curve (c) gives the predictions of Kloet and Lomon.

is different than it is for $pp \to pp\pi^0$ in the 400–600 MeV range, clear evidence for $T = 0$ inelasticity. We do not, however, find significant evidence for forward-backward asymmetry, which would be unambiguous evidence for $T = 0$ inelasticity. Our data here are in disagreement with the predictions of Kloet and Lomon.

B. Analyzing powers

Analyzing powers as functions of angular variables and p-p invariant mass slices are shown in Figs. 15–17. To conserve parity, A_{SO} and A_{LO} projected to θ and Ψ (Figs. 15 and 16) are expected to be zero. Thus, these results serve to act as a check on our analysis. In addition, A_{SO} and A_{LO} projected to χ_{pp} should be zero for χ_{pp} at 0° and 180°, in agreement with the data. The predictions from Kloet and Lomon for the analyzing powers are shown as the solid curves. There is marked disagreement with the data for the predictions A_{NO} projected to $\cos\theta$. Otherwise, the agreement with data is rather good, although the magnitude of the structure observed in A_{LO} projected to χ_{pp} is not well reproduced.

In order to understand the analyzing power data better, we have considered the partial waves which represent transitions from initial angular momentum states to final angular momentum states. The formalism for $NN \to NN\pi$ scattering was first clearly spelled out by Watson and Bruekner in 1951 [33]. Observables such as the analyzing powers can be understood in terms of products of helicity amplitudes M, which in turn can be written as linear combinations of partial wave amplitudes. In our partial wave description, we have characterized the final state by the relative angular momentum of the N-N system, and by the angular momentum of the pion with respect to the nucleon system. Each partial wave is labeled

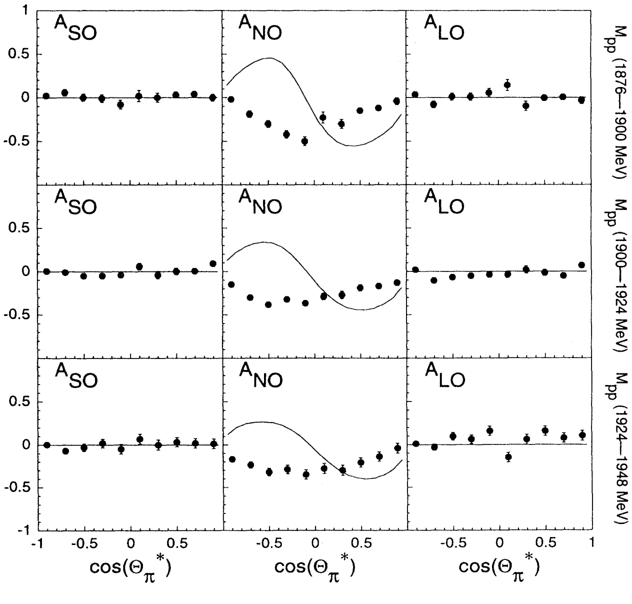

FIG. 15. Projected $np \to pp\pi^-$ analyzing powers as functions of angular variables and p-p invariant mass slices. A_{SO} and A_{LO} projected to $\cos\theta$ and φ are expected to be zero. The solid curves show the Kloet-Lomon predictions.

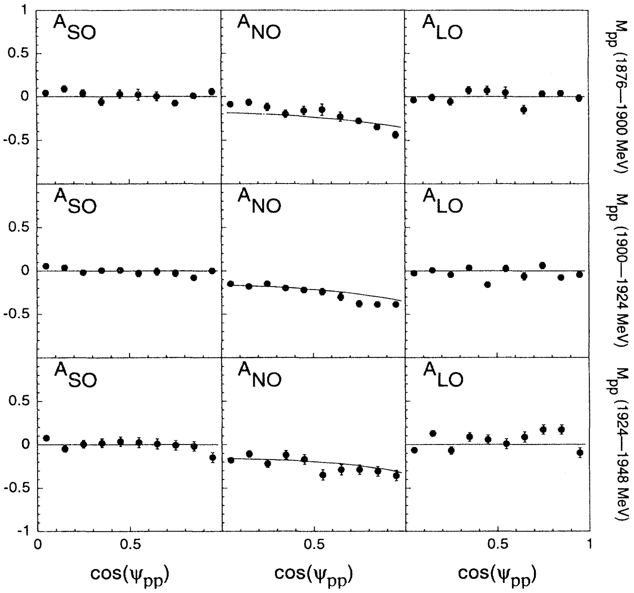

FIG. 16. See Fig. 15 caption.

$$^{2S+1}L_J \rightarrow {}^{2S'+1} L'_{J'} l_j$$

where S = spin of initial nucleons, L = orbital angular momentum initial nucleons, J = total angular momentum of partial wave, S' = spin of final nucleons, L' = orbital angular momentum of final nucleons, J' = total angular momentum of final nucleons, l = orbital angular momentum of pion, $j = J$, total angular momentum.

In each transition, total angular momentum (J), isospin (T), and parity must be conserved. In addition, since we have a system with two identical fermions in the initial state and two identical fermions in the final N-N state, the extended Pauli principle applies: only antisymmetric states are allowed. Thus, $L + S + T$ must be odd. For example, the transition $^3S_1 \rightarrow ^3 P_1 s_1$ is allowed if $T = 0$ (and not $T = 1$) in the initial state. Due to the rather small CMS energy (70 MeV) available to the final state particles in our experiment, we need consider only partial waves with small final state orbital angular momenta ($L' + l_\pi \leq 2$).

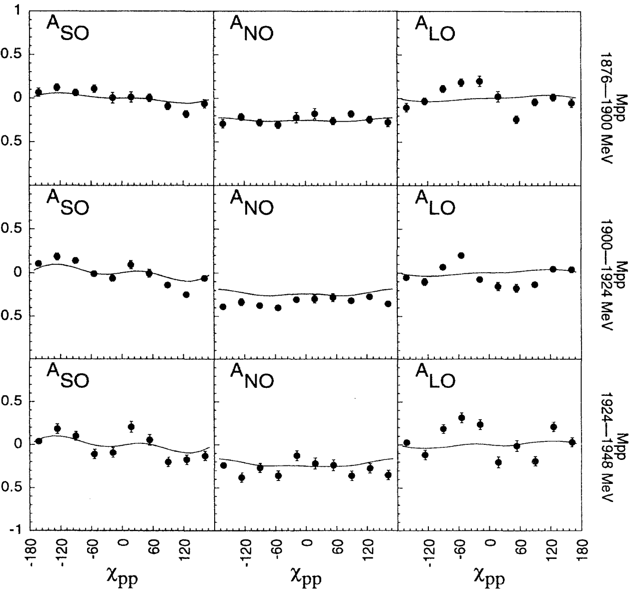

FIG. 17. See Fig. 15 caption.

Analyzing powers are sensitive to interferences between partial waves. Interference can only occur between partial wave amplitudes with the nucleons in the same final spin states. The total helicity amplitude M is written as a sum of the individual partial waves amplitudes:

$$M = \sum_k \eta_k e^{i\phi_k} F_k,$$

where each wave (k) has a characteristic inelasticity (η), phase shift (ϕ), and angular momentum decomposition (F) which contains the spherical harmonics, Clebsch Gordan coefficients, and Wigner rotation matrices. We can gain some insight into the roles of the partial waves by looking at the effects of simple interferences between selected waves. We have written a code, PWAVES, which accepts partial waves, inelasticity (η), and phase shifts (ϕ) as input, and then takes the appropriate traces of M to produce observables for specific points in phase-space. Although our data set is clearly insufficient for a full partial wave analysis, we hoped to be able to determine whether the observables demanded the presence of $T = 0$, as well as $T = 1$, amplitudes.

C. Discussion of A_{NO}

Measurements of A_{NO} show all-negative values over the pion CMS angle, θ (Fig. 15). This reflects the interference of waves from s-state and p-state pions, suggesting that partial waves of the type Ps and Pp are required (i.e., interferences such as $^1S_0 \rightarrow ^3P_0 s_0$ with $^3P_1 \rightarrow ^3P_0 p_1$), most of which have isospin 1. We had hoped that Ss, Sp, and Ps waves, all of which have isospin-0, and for which the A_{NO} versus $\cos\theta_\pi$ plots cross the axis would be all that was required. In such a case, the number of allowed partial waves would be very limited, and we could expect to see interferences of the type $^3D_1 \rightarrow ^1 S_0 p_1$ and $^3S_1 \rightarrow ^1 S_0 p_1$, both of which are $T = 0$ waves. Our observed A_{NO} data (Fig. 15) therefore does not require $T = 0$ inelasticity, and so can be expected to be similar to $pp \rightarrow pp\pi^0$ analyzing power data (pure $T = 1$).

Very little $pp \rightarrow pp\pi^0$ analyzing power data exists. By using the 450 MeV asymmetry and differential cross section data of Stanislaus [19] we have made an approximate estimate of A_{NO} versus $\cos\theta^*_\pi$ for his experiment. The results are shown in Fig. 18, and appear to be in rough agreement with our $np \rightarrow pp\pi^-$ analyzing power

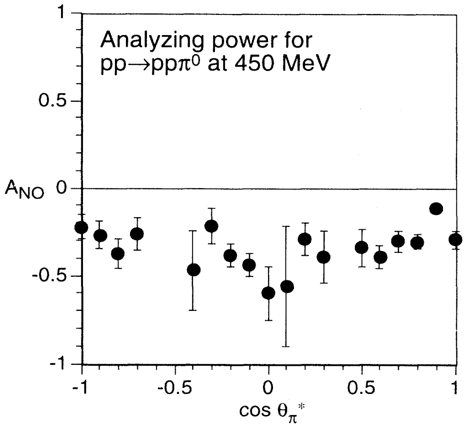

FIG. 18. Estimates of Stanislaus's analyzing power for $pp \rightarrow pp\pi^0$ at 450 MeV.

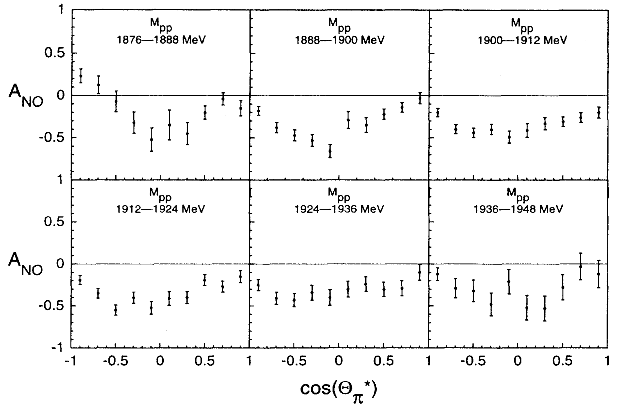

FIG. 19. Plot of analyzing power as a function of $\cos\theta^*$ and invariant p-p mass. The mass bin width is 12 MeV.

data. This apparent agreement in A_{NO} suggests no need for $T = 0$ amplitudes for most of phase space.

However, if we choose events from our data with small values of p-p invariant mass, we minimize the relative energies of the two protons, and should strongly enhance the probability that the two protons are emitted in a ${}^1S_0$ state. For the ${}^1S_0$ final two-proton state, $T = 0$ interferences from the partial waves ${}^3S_1 \rightarrow {}^1S_0p_1$ and ${}^3D_1 \rightarrow {}^1S_0p_1$ are strongly favored from angular momentum considerations. In Fig. 19 we show a plot of analyzing powers A_{NO} in narrow mass bins. For the smallest invariant mass slice the analyzing power is large and does cross the axis, evidence for interference of exactly the two ${}^1S_0p_1$ $T = 0$ partial waves above. In this respect our data are consistent with the data of the smallest invariant mass slice of Terrien *et al.* [25] at 572 MeV, shown in Fig. 20. In fact, our 443 MeV A_{NO} data show, overall, surprisingly close agreement with Terrien's data. Similar ${}^1S_0$ behavior was observed by Ponting *et al.* [34], in the scattering of polarized protons from a deuterium target. They observed π^- in coincidence with proton pairs emitted close together in the laboratory, thereby selecting preferentially those events with the final state protons in a relative S-state (${}^1S_0$). Their measured analyzing power, shown in Fig. 21, varies rapidly with pion CMS angle, and crosses the axis at a pion CMS angle between 70° and 75°. The slope of their data is opposite from the apparent slope of both our data and of Terrien's data, but this reflects only their choice of the proton as the beam particle, where we have chosen the neutron.

The model of Kloet and Lomon allows for pions only in relative p states, owing to their use of resonant intermediate states which are more appropriate at higher energies, and it is probable that the marked disagreement of our A_{NO} data with the Kloet-Lomon predictions is a strong indication that at 443 MeV (our energy), s-wave pions are also required.

D. Discussion of A_{SO}

Our measurements of A_{SO} show a behavior similar to $\sin 2\chi$, but with crossings of the axis at $\sim \pm 50°$. Interference between two partial waves would produce crossings at 90°. Consequently, at least three partial waves must interfere to produce the observed data.

E. Discussion of A_{LO}

At low p-p invariant mass, the A_{LO} data show a $\sin\chi$ dependence, whereas at higher p-p masses, there appears to be a $\sin 2\chi$ dependence. This data could be very useful in restricting partial wave combinations in a detailed partial wave analysis.

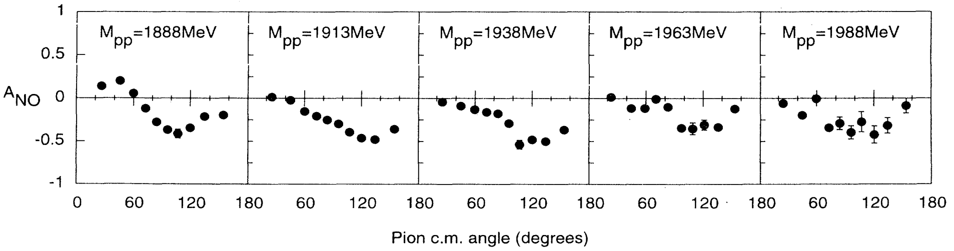

FIG. 20. Analyzing powers A_{NO}, from Terrien *et al.* at 572 MeV.

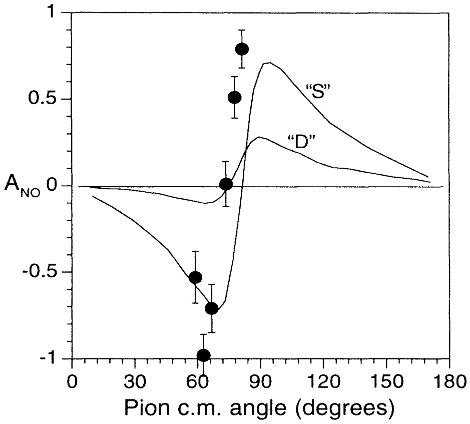

FIG. 21. A_{NO} data of Ponting *et al.* Solid lines are fits from partial wave analyses. The solution S has a large $^3S_1$ component in the initial state.

F. Conclusions

In summary, we have measured the relative differential cross section and first spin observables for the reaction $np \rightarrow pp\pi^-$ at 443 MeV. Our measurements have been compared with existing data and with predictions of the model of Kloet and Lomon. We can draw the following conclusions. (1) Our differential cross section data reveals a $\cos^2\theta$ dependence, evidence for $T = 0$ inelasticity. (2) Measurements of the analyzing power A_{NO} show all-negative values over the pion CMS angle θ, for all but the smallest invariant mass slice, suggesting no need for $T = 0$ amplitudes for most of phase space. For the smallest invariant mass slice, the analyzing power is large and does cross the axis, evidence for interference of $T = 0$ partial waves in this region of phase space. (3) Some of the variables show marked disagreement with predictions of the model of Kloet and Lomon; for other variables, there is surprisingly good agreement. We hope that our measurements will help to provide direction for the development of a unified model of the N-N interaction below and above pion threshold. Additional spin data, such as spin correlation observables, would allow much more detailed partial wave analyses and would provide more stringent tests of theoretical models.

ACKNOWLEDGMENTS

We gratefully acknowledge the talented support of the TRIUMF technical staff, the source group, and W. Kellner of the cryogenic targets group. We are also grateful to Dr. D. V. Bugg for very enlightening and helpful comments on the analysis and interpretation of our results. We thank Dr. W. Kloet and Dr. E. Lomon for providing us with their T matrices. The experiment was supported by grants from the U.S. Department of Energy, the National Science Foundation, and National Sciences and Engineering Research Council of Canada.

---

[1] W. M. Kloet and R. R. Silbar, Nucl. Phys. **A338**, 281 (1980); Phys. Rev. Lett. **45**, 970 (1980); T.-S. Lee, *ibid.* **50**, 1571 (1983); E. van Faassen and J. A. Tijon, Phys. Rev. C **30**, 285 (1984); F. Sammarucca and T. Mizutani, *ibid.* **41**, 2286 (1990); Ch. Elster, K. Holinde, D. Schutte, and R. Machleidt, *ibid.* **38**, 1828 (1988); W. M. Kloet and E. L. Lomon, *ibid.* **43**, 1575 (1991); T.-S. H. Lee and D. O. Riska, Phys. Rev. Lett. **70**, 2237 (1993).
[2] J. Dubach, W. M. Kloet, and R. R. Silbar, Nucl. Phys. **A466**, 573 (1987).
[3] A. H. Rosenfeld, Phys. Rev. **96**, 139 (1954).
[4] L. Van Howe, R. Marshak, and A. Pais, Phys. Rev. **88**, 1211 (1952).
[5] J. Bystricky *et al.*, J. Phys. (Paris) **48**, 1901 (1987).
[6] S. Mandelstam, Proc. R. Soc. London **A244**, 491 (1958).
[7] B. J. VerWest and R. A. Arndt, Phys. Rev. C **25**, 1979 (1982).
[8] G. B. Yodh, Phys. Rev. **98**, 1330 (1955).
[9] A. P. Batson, B. B. Culwick, H. B. Klepp, and L. Riddiford, Proc. R. Soc. London **A251**, 233 (1959).
[10] M. Kazarinov and N. Simonov, Sov. Phys. JETP **25**, 56 (1959).
[11] R. Handler, Phys. Rev. **138**, 1230 (1965).
[12] V. P. Dzhelepov *et al.*, Sov. Phys. JETP **23**, 993 (1966).
[13] M. Kazarinov and N. Simonov, Sov. J. Nucl. Phys. **4**, 100 (1967).
[14] A. Abdivaliev *et al.*, Nucl. Phys. **B99**, 445 (1975).
[15] M. Kleinshmidt *et al.*, Z. Phys. A **298**, 253 (1980).
[16] W. Thomas *et al.*, Phys. Rev. D **24**, 1736 (1981).
[17] L. G. Dakhno *et al.*, Phys. Lett. **114B**, 409 (1982).
[18] H. Fischer *et al.*, SIN Newsletter **20**, NL15 (1988).
[19] S. Stanislaus, Ph.D. thesis, University of British Columbia, 1987 (unpublished); S. Stanislaus *et al.*, Phys. Rev. C **44**, 2287 (1991).
[20] A. F. Dunaitsev and Yu. D. Prokoshkin, Zh. Eksp. Teor. Fiz. **36**, 1656 (1959) [Sov. Phys. JETP **9**, 1179 (1959)].
[21] R. A. Stallwood *et al.*, Phys. Rev. **109**, 1716 (1958).
[22] F. Shimizu *et al.*, Nucl. Phys. **A386**, 571 (1982).
[23] J. Marshall *et al.*, Phys. Rev. **88**, 632 (1952).
[24] D. V. Bugg, Annu. Rev. Nucl. Part. Sci. **35**, 295 (1985).
[25] Y. Terrien *et al.*, Phys. Rev. Lett. B **294**, 40 (1992).
[26] M. Bachman, Ph.D. thesis, University of Texas, 1993 (unpublished).
[27] L. Buchmann *et al.*, Nucl. Instrum. Methods Phys. Res. Sect. A **306**, 413 (1986).
[28] W. D. Ramsay *et al.*, Nucl. Instrum. Methods Phys. Res. Sect. A **327**, 265 (1993).
[29] D. V. Bugg, Nucl. Phys. **A467**, 575 (1987).
[30] R. Arndt, Scattering Analysis Interactive Dialup (SAID) program, Virginia Polytechnic Institute, 1993; Phys. Rev. D **28**, 97 (1983).
[31] R. L. Shypit *et al.*, Phys. Rev. C **40**, 2203 (1989).
[32] W. M. Kloet and E. Lomon, private communication.
[33] K. M. Watson and K. A. Brueckner, Phys. Rev. **83**, 1 (1951).
[34] C. Ponting *et al.*, Phys. Rev. Lett. **63**, 1792 (1989).

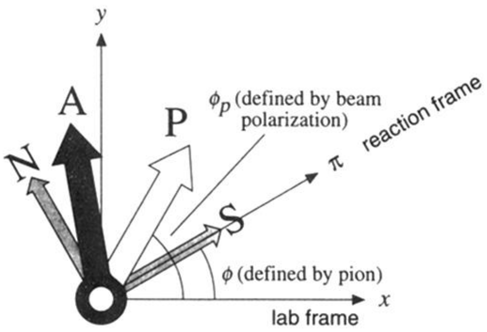

FIG. 12. The coordinate system and angles used in the calculation of asymmetries.

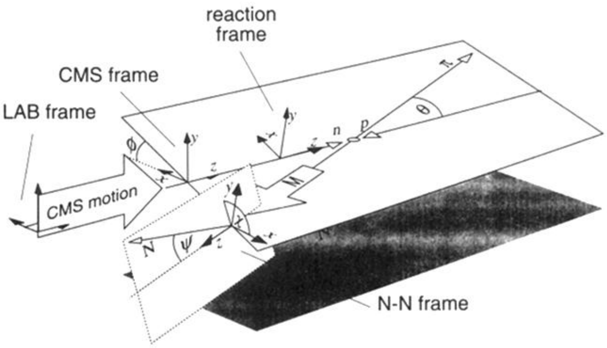

FIG. 13. The kinematic variables used in defining and binning the observables.

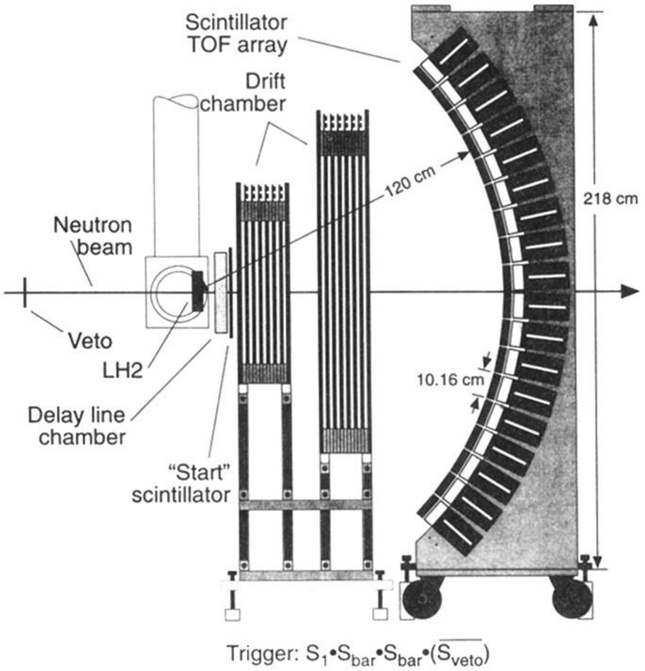

FIG. 6. A schematic diagram of our $np \rightarrow pp\pi^-$ detector at TRIUMF.

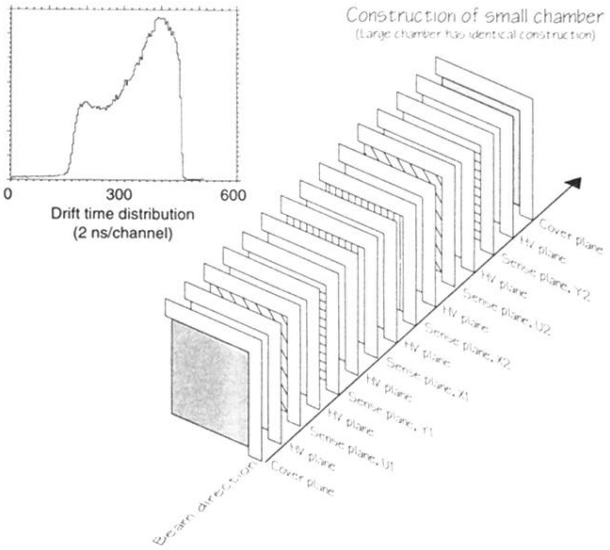

FIG. 9. Time distribution and layout of the *E*372 drift chambers.